# Evaluation of the mechanical performance of polymer parts fabricated using a production scale multi jet fusion printing process

**Heather J. O' Connor, Andrew N. Dickson, Denis P. Dowling**

School of Mechanical and Materials Engineering, University College Dublin, Belfield, Dublin 4, Ireland

*** Correspondence:** Email: heather.oconnor@ucdconnect.ie

## Abstract

Additive manufacturing (AM) is rapidly becoming one of the most popular manufacturing techniques for short run part production and rapid prototyping. AM encompasses a range of technologies, including powder bed fusion (PBF) process. The purpose of this paper is to evaluate and benchmark the mechanical performance of polyamide 12 (PA12) parts, fabricated using a production scale powder bed fusion printing process (HP Multi Jet Fusion printing process). This system has a build volume is 380 x 254 x 350 mm. The printed polymer parts were examined to determine their hydrophobicity, morphology, porosity and roughness. Chemical and thermal properties of the PA12 parts were also evaluated using attenuated total reflection infrared spectroscopy (ATR FT-IR), x-ray photoelectron spectroscopy (XPS) and differential scanning calorimetry (DSC). The study highlights the influence of build orientation on the tensile (ISO 527-1:2012) and flexural (ISO 178:2010) properties. In terms of tensile strength, the parts exhibited isotropic behaviour with a maximum tensile strength of 49 MPa. In terms of flexural testing, the build orientations had a significant effect on the strength of the printed part. The Z orientation exhibited a 40% higher flexural strength, when compared to that of the X orientation. The maximum flexural strength observed was 70 MPa. The results of this rapid, production scale AM study are compared with previous studies that detail the mechanical performance of PA12, fabricated using PBF processes, such as selective laser sintering.

## 1. Introduction

Additive manufacturing (AM), also known as three-dimensional (3D) printing, is a process where parts are generated layer by layer [1, 2]. There are seven categories of AM material processing: binder jetting, directed energy deposition, material extrusion, material jetting, powder bed fusion, sheet lamination and vat photopolymerization [3]. Quinlan et al. illustrates how many of these processes have an overall low build rate and often a low resolution in comparison with typical moulding and machining processes [4]. In addition to this, the mechanical performance of material extruded AM parts, rarely matches the performance of conventional manufacturing methods such as injection moulding [5, 6]. To speed up build-time without sacrificing the strength and quality of the print, new AM technologies have recently emerged. One such technology, developed by HP is called the Multi Jet Fusion printing process (MJF™) [7]. This production scale AM processing technology, involves the use of powder bed fusion, in which the polymer particles are heated and fused to fabricate the printed parts. There has already been a small number of reports of industrial applications of this technology, for example for the fabrication of customised automotive parts [8].

The polymer used with the MJF™ process is polyamide 12 (PA12), which is by far the most widely used for powder bed fusion AM [9, 10]. Its melt temperature is considerably higher than its crystallisation temperature, allowing the crystallisation process to be delayed during the build process, thus reducing the accumulation of residual stresses and distortions [11]. In some cases, the PA polymer is combined with additional agents such as silicon carbide, glass beads, aluminium, carbon nanotubes and nanofibers to enhance the printed parts mechanical properties [12-16]. PA polymer powders that are currently reported by the manufacturer to be compatible with the MJF™ process are: polyamide 12, polyamide 11 and polyamide 12 with glass beads.

A number of authors have reported on the physical, mechanical and chemical properties of printed PA12 parts [11, 17-19] fabricated using PBF processes. Griessbach et al. [18] for example reported that for a selective laser sintering (SLS) process, there was a linear correlation between increasing part density and its tensile strength (values obtained were in the range 33 – 50 MPa). It was observed that as the PA12 crystallinity in the fabricated part increased, that the percentage elongation at break was found to decrease from 15% (24% crystallinity) to 5% (29% crystallinity). Drummer et al [19] found a similar correlation for SLS printed parts, with higher part tensile strength the PA12 crystallinity increased. They also reported that their AM sintered parts exhibited a higher mechanical performance, when compared to injection moulded parts, fabricated using the same powder. Ellis et al [17], investigated the relationship between PA12 part print density and its crystallinity through a process similar to MJF™, called high speed sintering (HSS). As for the SLS printed parts discussed earlier, it was observed that as the crystallinity of the polymer increased the tensile strength increased while there was a decrease in elongation.

As illustrated schematically in Figure 1, the MJF™ process begins with the deposition of a layer PA powder onto a build platform. A proprietary fusing agent is selectively applied to the powder bed, this consists of a black ink which contains an infrared absorbing agent. In addition, a detailing agent is applied to the powder bed, its role when applied around the contours of the part, is to prevent fusion of the particles and to improve resolution. The polymer heating is achieved by passing planar infrared lamps over the powder bed. The fusing agent absorbs the IR radiation and converts it to thermal energy, which in turn sinters and fuses the build material. The fused polymer forms a layer and the process is repeated layer by layer as the build plate move down, building up the 3D part [20]. Compared with alternative powder bed fusion technologies such as selective laser sintering (SLS), the MJF™ process is much more rapid as it involves the use of planar IR radiation treatments, as opposed to the more widely applied point-wise fusion technique [7].

This paper aims to evaluate the mechanical performance and print characteristics, such as crystallinity of PA12 polymer parts fabricated HP Jet Fusion 3D 4200 printer. To the authors knowledge this is the first study to evaluate the mechanical performance of polymer parts fabricated using this production scale powder bed fusion technique.

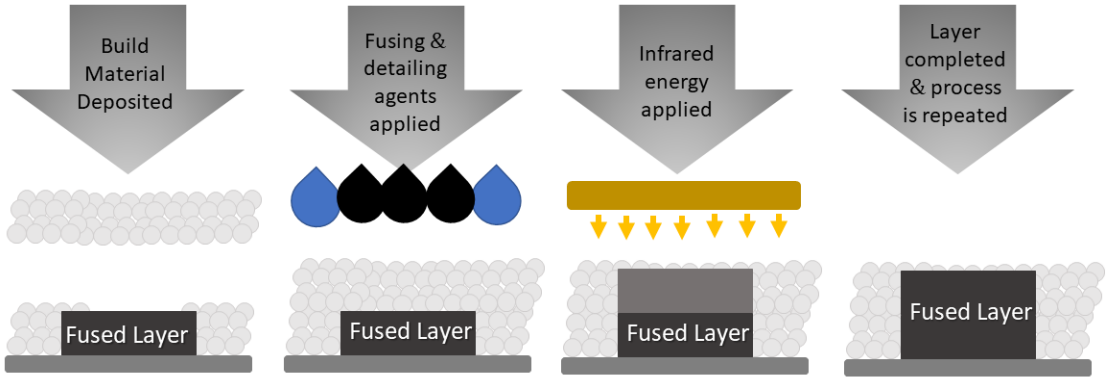


Figure 1: Schematic of the MJF™ Process, involving the application of the polymer powder layer, followed by the fusing and detailing agent. Exposure to IR causes the particles to fuse in the region where the agents had been applied. The process is then repeated [7].

## 2. Experimental methods

This study was carried out on parts fabricated using a HP Jet Fusion 3D 4200 printer. The printing process consists of two units; the 3D printer and the post-processing station (Figure 2). Parts and powder are transferred using the modular build unit between the printer and the post-processing station. The available build volume is 380 x 254 x 350 mm. The print mode used was balanced – which was designed to allow a good compromise between the mechanical strength and young's modulus. All parts were centred in the build volume, with a space of 10 to 20 mm separating each part to allow complete thermal flow. The total printing time of 108 parts, which had an approximate total volume of 388,164 $mm^3$, and took 7.5 hours to print. Parts were fabricated using PA12 powder sourced from HP, along with their detailing and fusing agents. Test coupons were fabricated with the dimensions given in Table 1. After printing, the parts were allowed cool in the powder bed for 16 hours before being un-packed. Loose powder was removed from the parts using compressed air before being brushed using a hard bristle brush, to further remove excess powder.

Table 1: Mass and dimensions of printed coupons pre- and post-processing.

| | **Thickness (mm)** | **Length (mm)** | **Breadth (mm)** | **Weight (g)** |
|---|---|---|---|---|
| **Coupon as printed** | 2.24 ± 0.06 | 25.06 ± 0.10 | 25.02 ± 0.07 | 1.26 ± 0.01 |
| **Coupon (glass-bead blasted)** | 2.08 ± 0.03 | 24.95 ± 0.08 | 24.98 ± 0.11 | 1.24 ± 0.01 |

Figure 2: HP Jet Fusion 3D 4200 (left) and HP Jet Fusion 3D processing Station (right) [7]

The printed coupons were then abraded using a Guyson Euroblast 6 blasting cabinet and glass beads (55 – 90 µm, Honite 18), to remove loosely bound polymer material. The dimension and weight of the resulting parts are given in Table 1. The part weight was obtained using a Sartorios MC1 Analytic AC 210 S balance and the part dimensions were measured using a digital vernier callipers, Digi Plus-Line – Vogel Germany GmbH & Co.KG.

*2.1 Print characterisation*

The hydrophobicity and surface energy of the finished coupons was determined using an OCA 20 from Dataphysics Instrument. The sessile drop technique was employed using static measurements of made with 1µl of deionised water. Surface energy measurements were obtained using the Owens, Wendt, Rabel and Kaelble technique (OWRK) [21], using deionised water, diiodomethane and ethylene glycol as test liquids.

The morphology of the printed parts was firstly examined using microscopy (VHX – 5000 Keyence Microscope), as well as using a Tabletop Hitachi tm 1000 SEM. Prior to examination using the latter technique, a thin layer of a conductive gold coating was applied by sputtering. To evaluate porosity, cross sectional analysis was performed under using optical microscopy. An Olympus microscope was used to image 20 locations on the cross sections (50 X magnification), of 4 test samples (5 images / sample). Images were then converted to greyscale and passed through a threshold filter to quantify areas of air void (typically identified as solid black, in contrast to the light grey of the polymer). This was facilitated by ImageJ analysis software and porosity was expressed as a percentage. Surface roughness measurements were carried out using a Wyko NT1100 optical profilometer in vertical scanning interferometer mode (VSI). The system was used to calculate the arithmetic average roughness $R_a$. The magnification used was 25 X, with a sample size of 91.3 × 120 µm.

The chemistry of the polymer coupons was evaluated using attenuated total reflection infrared spectroscopy (ATR FT-IR) and x-ray photoelectron spectroscopy (XPS). FT-IR spectra of the printed polymers were obtained using a Nicolet iS50 FTIR Spectrometer, Wavenumber range: 8000 - 650 $cm^{-1}$, diamond ATR. To avoid any interference from contamination, the specimen was sliced open and the freshly cut side was used for measurements. The thermal properties of the printed polymer were examined using differential scanning calorimetry (DSC). These measurements were carried out using a Netzsch DSC214 system, with a heating rate of 10 K $min^{-1}$ under nitrogen. The glass transition temperature was evaluated according to the half-step method (DIN 51007). The percentage crystallinity ($X_m$) was calculated using equation 1, where the enthalpy of fusion ($\Delta H_m$) was obtained from integrating the melting peak area using Proteus evaluation software and the heat of fusion of 100% crystalline PA12, $\Delta H_m^0$, was taken as 209.3 J $g^{-1}$ [11, 16].

$$X_m = \frac{\Delta H_m}{\Delta H_m^0} \times 100 \qquad \text{Equation 1}$$

X-ray photoelectron spectroscopy (XPS) analysis is carried out using Kratos-Axis DLD photoelectron spectrometer at a pressure of $5.4 \times 10^{-8}$ mbar. 1.486 keV. Monochromatic Al $K_\alpha$ line is used as the X-ray source at operation conditions of 15 kV and 10 mA. The binding energy was referenced to the C 1s peak at 248.8 eV.

*2.2 Mechanical performance*

A mechanical performance evaluation of the printed PA12 was conducted to investigate isotropy of the printed parts. This was carried out by printing in three build orientations; X, Y and Z, as illustrated schematically in Figure 3. Tensile (ISO 527-1:2012) [22] and Flexural (ISO 178:2010) [23] tests were conducted on at least five parts for each orientation, using Zwick Roell z005 mechanical tester, with a 10 kN load cell and manual wedge grips. A tensile strength study was performed on type CP dogbone geometry according to ISO 20753:2014. The specimens were tested under a preload of 0.1N, at a crosshead speed of 1 mm/minute and evaluated with a video extensometer. Subsequent to tensile testing, the specimens were examined using SEM (TM-1000 Hitachi). Flexural tests were performed on parts with the dimensions of 80 × 10 × 4 mm, with a preload of 1 N and a crosshead speed of 2 mm/minute, as per ISO 178 standard. Specimens were tested to maximum deflection of 15 mm. No sample experienced total failure and all returned almost completely elastically to their original shape after load was retracted.

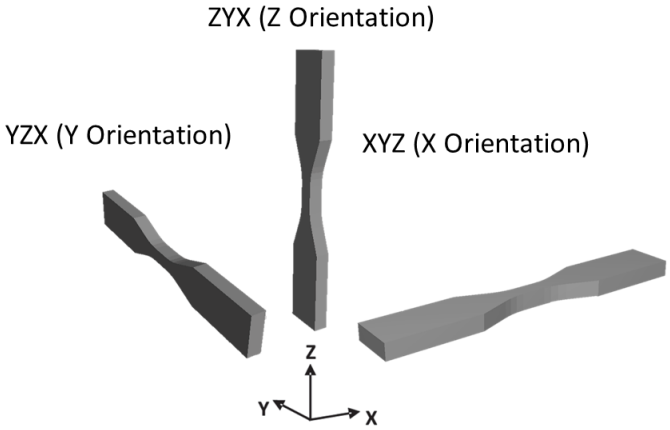


Figure 3: Schematic of build orientation axes according to ISO/ASTM 52921

## 3. Results and discussion

### *3.1 Print characterisation*

Microscopy images showing the morphology of the printed PA12 coupons, pre- and post- glass bead blasting treatment are given in figure 4. The as-printed coupons had partially melted PA12 powder particles still bound to the surface of the printed test coupon. These particles had typical diameters in the range 50 to 80 µm. Once removed using glass bead blasting, the PA12 coupons exhibited a rough, grainy morphology.

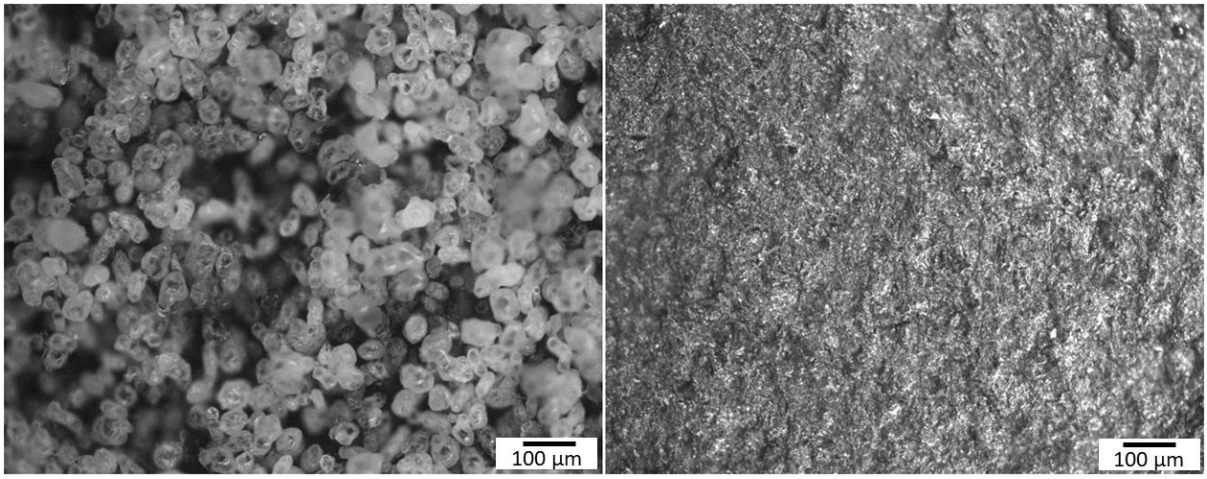


Figure 4: Microscopy of PA12 coupons with a loosely bound particle layer as (left – as printed) and after glass bead blasting (right). Scale bar 100µm.

The results of the investigation of the hydrophobicity, surface energy and roughness of the glass-bead blasted coupons are detailed in table 2. The water contact angle and surface energy values obtained are typical of PA 12 [24]. The roughness of the finished coupon ranged from 2.5 – 10.3 µm, depending on which face of the coupon was being evaluated. In the case of all printed parts, the side of the part facing down, (the initial layer fused), was smooth in comparison to the side facing up (the last layer fused).

Table 2: Water contact angle, surface energy and roughness of glass-bead blasted coupons.

| | **WCA (°)** | **SE (mJ/m$^2$)** | **Polar (mJ/m$^2$)** | **Disp. (mJ/m$^2$)** | **Roughness, $R_a$ (µm)** |
|---|---|---|---|---|---|
| **Coupon** | 79 ± 5 | 37 ± 2 | 4 ± 2 | 33 ± 2 | 2.54 ± 0.42 (smooth)<br>10.29 ± 2.82 (rough) |

Cross sectional analysis was performed using optical microscopy on parts cut using a surgical blade. The average porosity observed within these parts was calculated using ImageJ Analysis Software and was found to be 3.2 ± 4.1 %, based on the analysis of 4 coupons, printed in the X orientation. The pores were found to be randomly distributed, with no correlation found between the porosity level within different regions of the coupons i.e. edge or centre. This level of porosity is comparable to the < 5%, percentage porosity obtained by Van Hooreweder et al. for SLS printed parts [25].

The PA12 coupons were partially cut and then sheared, the latter section was then examined using SEM. The resulting images as shown in Figure 5 of the shear fractured surfaces, demonstrate the fused particulate nature of the build. An example of a pore is also demonstrated in this figure.

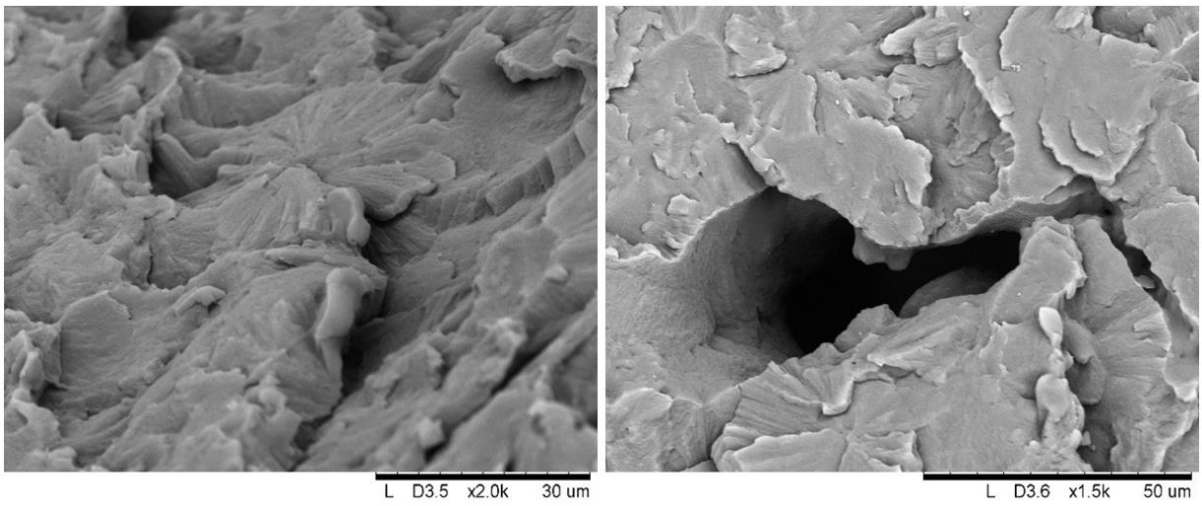


Figure 5: Micrograph of the shear fracture surface of the PA12 coupon demonstrating the fused particulate structure (left). An example of an isolated pore observed in the polymer structure (right).

*3.2 Chemical and thermal analysis*

Figure 6 provides an example of an infra-red (ATR-IR) spectrum of a printed PA12 coupon which had been sectioned. The spectral peaks as detailed in Table 3 exhibited a close correlation with those for PA12 reported in the literature [26].

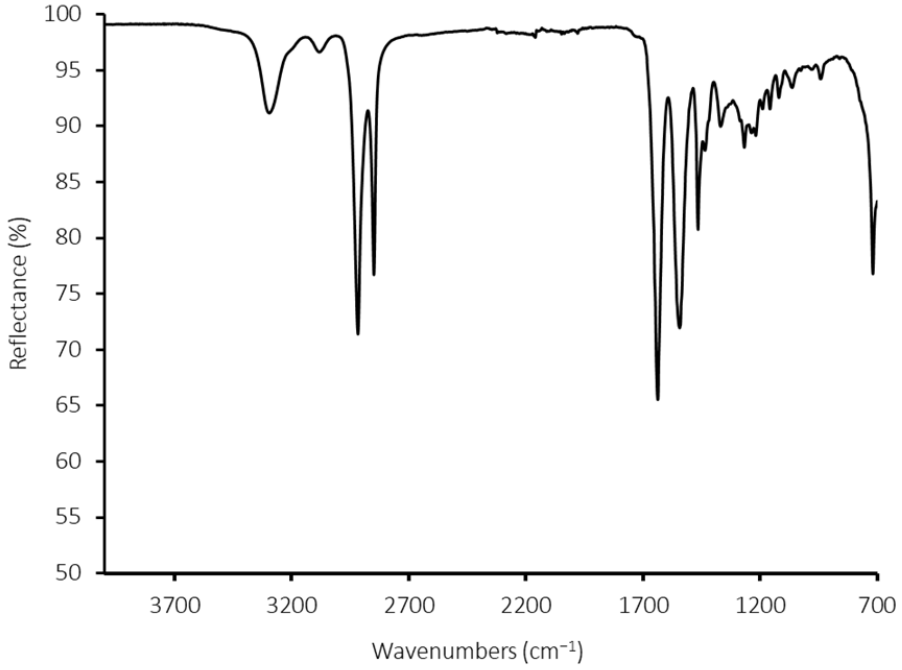


Figure 6: ATR-IR spectrum of the printed PA12.

Table 3: ATR-IR peak assignments for Figure 6

| **FTIR peaks ($cm^{-1}$)** | **Peak assignments** |
|---|---|
| 3297 | Hydrogen-bonded N−H stretching |
| 2918 | $CH_2$ asymmetric stretching |
| 2850 | $CH_2$ symmetric stretching |
| 1639 | C=O stretching |
| 1545 | C–N stretching + C=O in plane bending |
| 1370 | CH bend, $CH_2$ twisting |
| 1269 | C–N stretching + C=O in plane bending |
| 1122 | C−C stretching |
| 944 | CONH in plane |
| 720 | $CH_2$ rocking |

The thermal properties of the printed polymer parts were examined using DSC (Figure 7). The resulting data provided information on the temperature transitions, melting range and the degree of crystallinity as detailed in Table 4. The negative (endothermic) peak in the thermogram is associated with melting as more heat flow is needed. The melting temperature of the material ranged from 182 – 185 °C and on cooling, the crystallisation peak occurred between 147 – 148 °C. This wide supercooling region (the temperature difference between then endothermic and exothermic peaks), is characteristic of PA12 and a desirable property, making PA12 a commonly used powder in SLS [19]. The percentage crystallinity, $X_m$, was obtained by integrating the melting peak area to find the melting enthalpy ($\Delta H_m$) and using equation 1, taking 209.3 J/g for the enthalpy of fusion for 100% crystalline

PA12 [16]. This gave an average crystallinity of 32%. The melting and cooling data obtained from DSC (Table 4) corresponds well with the thermal analysis carried out on PA12 SLS fabricated parts [11, 19]. Salazar et al. reported a melting point at 183°C ($T_m$) and a percentage crystallinity ($X_m$) of 34% for SLS fabricated PA12. XPS analysis was performed on a sample of the printed PA12, taken from the centre of a coupon in order to avoid contamination (Fig. 8). The XPS survey spectra gave peaks at 89, 154, 285, 350, 400, 532, 690 and 1072 eV which corresponds to Mg, Si, C, Ca, N, O, F and Na respectively (Table 5).

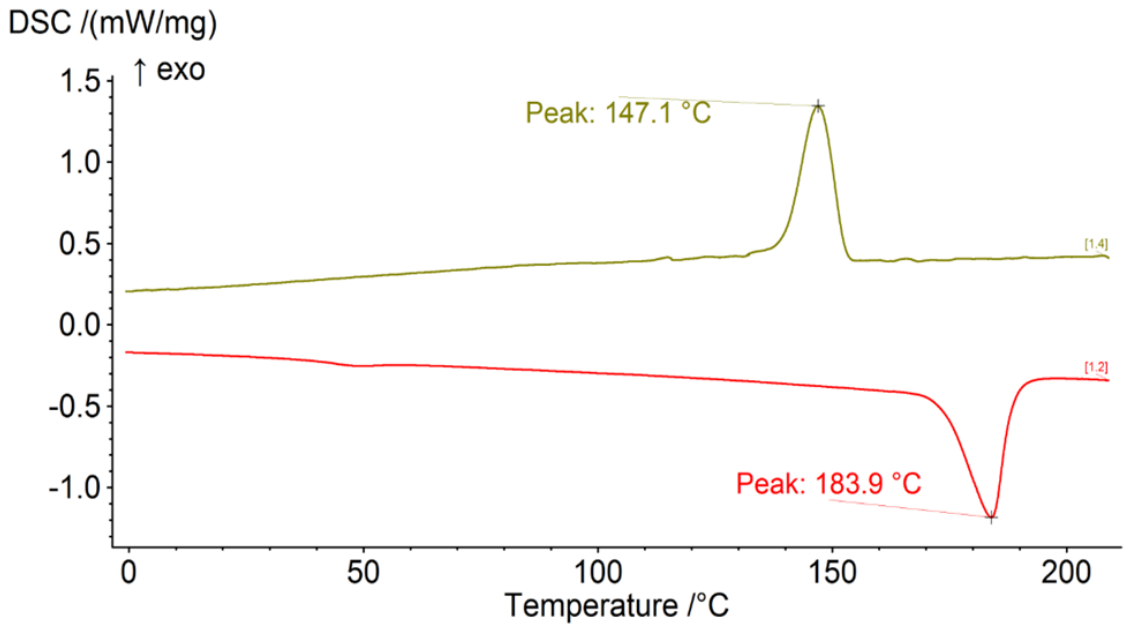


Figure 7: DSC thermogram of PA12

Table 4: Thermal properties of the PA12 (mean obtained from three test samples)

| | **Heating** | | **Cooling** | |
|---|---|---|---|---|
| $T_g$ (°C) | $T_m$ (°C) | $X_m$ (%) | $T_c$ (°C) | $X_c$ (%) |
| 44 | 184 | 32 | 147 | 26 |

Table 5: XPS analysis results showing the elemental concentrations obtained for the PA12 parts

| | **Elemental composition (%)** | | | | | | | |
|---|---|---|---|---|---|---|---|---|
| **Printed PA12** | C (1s) | O (1s) | Si (2s) | N (1s) | Na (1s) | Mg (2s) | Ca (2p) | F (1s) |
| | 77.45 | 15.55 | 2.59 | 2.59 | 0.95 | 0.7 | 0.5 | 0.26 |

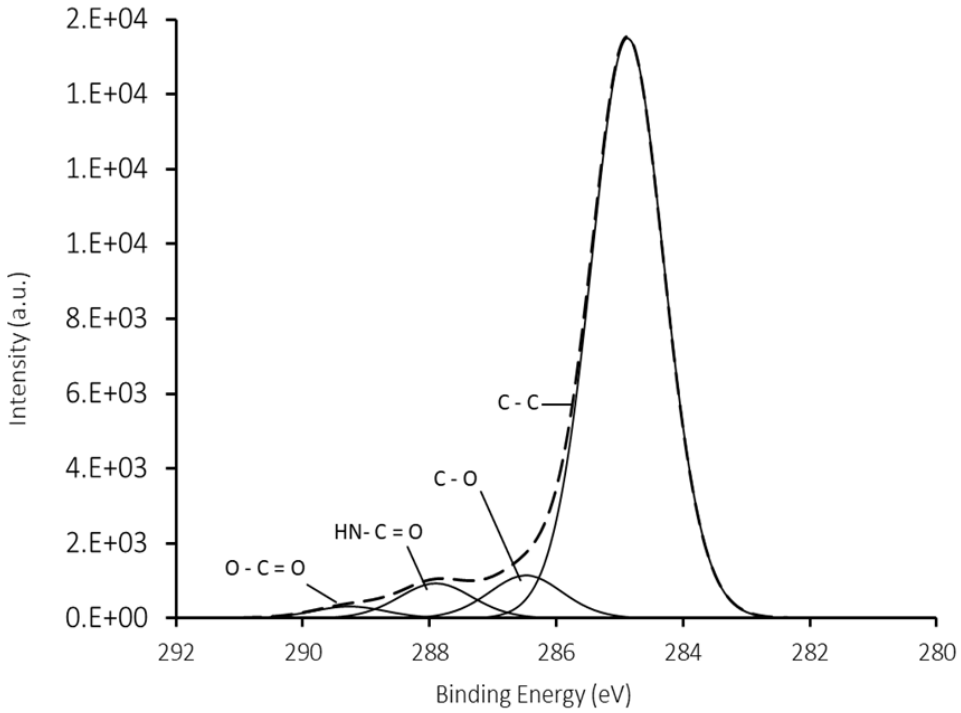


Figure 8: High resolution scans of C 1s oxidation states of the PA12 printed coupon

*3.3 Mechanical performance*

The mechanical performance of the PA12 printed specimens was evaluated based on tensile and flexural strength measurements, according to ISO 527 and ISO 178. Table 6 details the tensile properties of PA12 dogbones printed in the X, Y and Z orientation. No significant difference in tensile strength was observed between the three orientations. The specimen printed in the Y orientation exhibited a lower tensile modulus and a significant increase in the percentage elongation at break, from 19% to 27%, when compared to that of the X orientation. Figure 9 gives a typical stress strain curve for the three orientations, demonstrating the higher percentage elongation at break of the specimen printed in the Y orientation. All specimen broke in the centre of the dogbone geometry and exhibited similar failure mechanisms independent of the build orientation. After tensile testing, the fractured parts were examined. As illustrated in the SEM micrographs given in Figure 10, ductile deformation was observed at the fracture interface. It is interesting to note, that the level of polymer ductility, demonstrated in Figure 10, is substantially greater than that reported by a number of authors for fractured polyamide produced by other PBF processes [27, 28].

Table 6: Average tensile test results, giving tensile modulus ($E_t$), strength ($\sigma_y$) and elongation at break ($\varepsilon_b$ ).

| **Build Orientation** | **$E_t$ (Tensile Modulus) MPa** | **$\sigma_{max}$ (Tensile Strength) MPa** | **$\varepsilon_b$ (Elongation at Break) %** |
|---|---|---|---|
| **X** | 1242 ± 28 | 47 ± 0.9 | 19 ± 2.8 |
| **Y** | 1147 ± 40 | 48 ± 0.8 | 27 ± 1.2 |
| **Z** | 1246 ± 37 | 49 ±0.6 | 16 ± 1.9 |

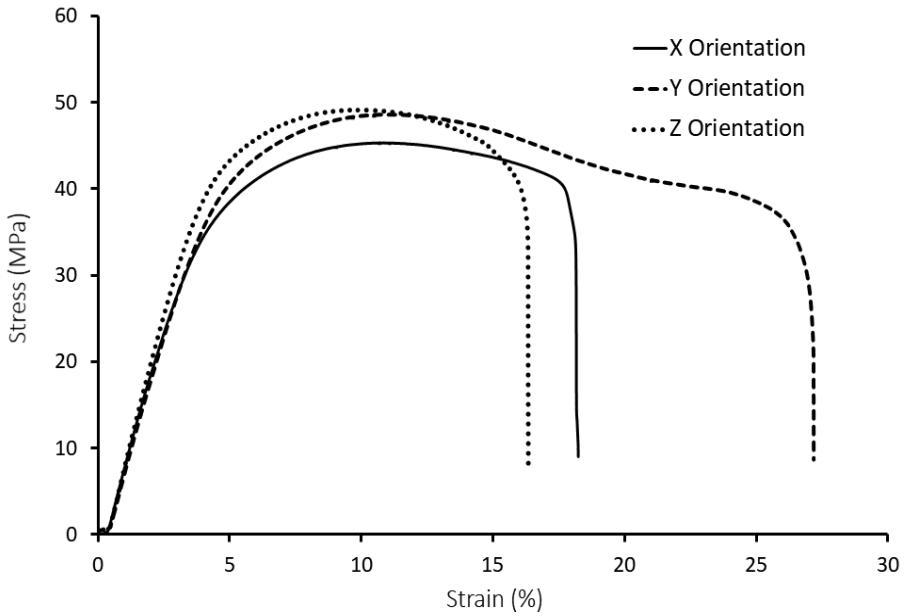


Figure 9: Tensile stress strain curves of printed PA12 for X, Y and Z build orientations.

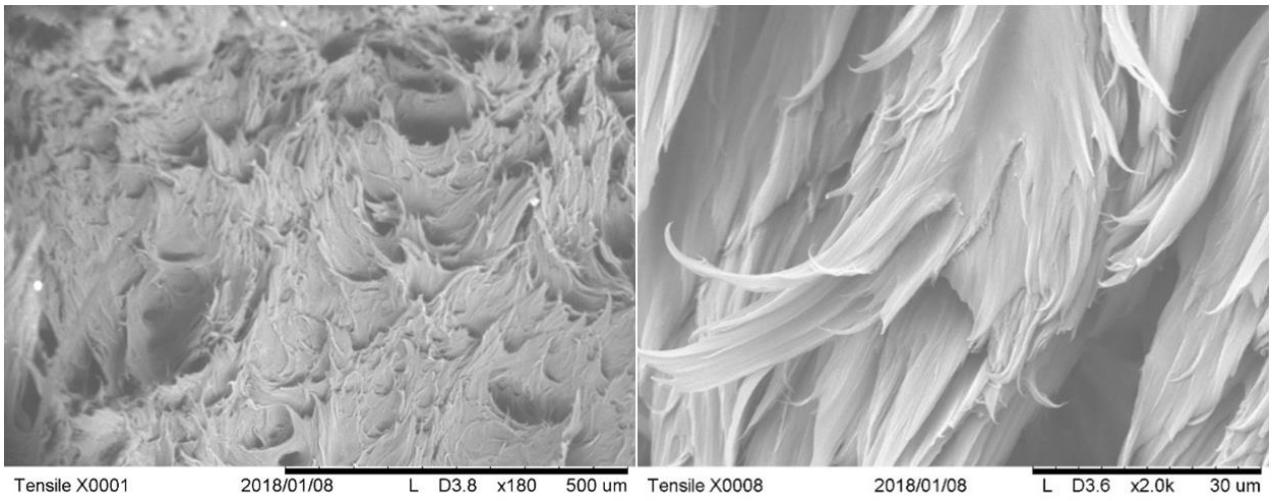


Figure 10: Micrographs of the tensile fracture surface, demonstrating the ductile nature of the fractured PA12 polymer.

The flexural strength and modulus of the PA12 parts are detailed in Table 7, while the flexural stress strain curves for the three build orientations are given in Figure 11. The flexural strength of the PA12 printed parts range from 50 – 70 MPa, depending on the build orientation. The Y orientation exhibited a 31% increase in flexural strength when compared to the X orientation and the Z exhibited a further 5% increase, when compared to the strength of the Y orientation. A similar trend was observed when comparing the flexural modulus, with a 37% increase when comparing the X and Y build orientations, and a further increase in 8% when comparing the Z, with the Y orientation.

Table 7: Flexural strength and modulus according to ISO 178

| Build Orientation | $\sigma_f$ (Flexural Stress) MPa | $E_f$ (Flexural Modulus) MPa |
|---|---|---|
| **X** | 50 ± 0.9 | 1146 ± 51 |
| **Y** | 66 ± 0.5 | 1567 ± 36 |
| **Z** | 70 ± 0.7 | 1687 ± 12 |

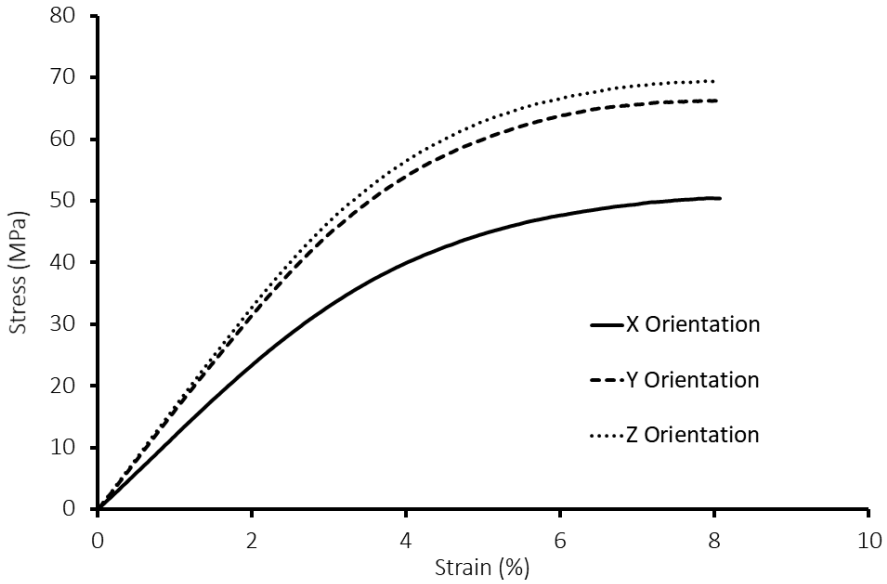


Figure 11: Flexural stress strain curves of printed PA12 for X, Y and Z build orientations.

It is concluded from this study that there was a general trend of strength increasing in the following build orientation: Z > Y > X. Strength variation with part orientation is also observed in parts fabricated by similar PBF processes. For the SLS parts however, the Z orientation is usually the weakest [27, 29, 30], as stress is applied perpendicular to the layer to layer bonding [31]. For the MJF™ printed polymers, a factor that may explain the higher strength observed along the Z orientation, is the additional weight of the layers as the thickness is increased in the Z direction. This may facilitate a denser and less porous print.

Previous authors have highlighted, that the degree of particle melting can significantly influence the mechanical properties of the printed polymer [32]. A further factor to note when examining the results presented in Tables 6 and 7 and Figures 9 and 11, is the relatively low level in strength variation obtained at each orientation, indicating a relatively homogeneous level of part fusion at various locations across the test bed.

The chemical characterisation of the PA12 grade used in the MJF™ system is typical of other PA12 polymer's in terms of chemical functionality and thermal properties. Having obtained the mechanical

test results, it is now useful to benchmark parts printed using the MJF™ system with other powder bed fusion systems as reported in the literature. Table 8 makes this comparison based on tensile strength measurements reported for PA12 parts. It should be noted that due to variables such as material grade, process parameters, mechanical testing parameters and type of powder bed fusion process used, a fully quantitative, direct comparison cannot be made between the studies. Based on this comparison however, it is clear that PA12 parts printed using the production scale MJF™ process exhibit a mechanical performance comparable with those using the other production scale powder bed fusion processes.

Table 8: A comparison of the tensile properties of PA12 parts, fabricated by powder bed fusion processes. Where $\sigma_{Max}$ is the maximum tensile strength, $E_t$ is the tensile modulus and $\varepsilon_b$ is the percentage elongation at break.

| **PA12 Powder/ Powder Bed AM Machine** | **$\sigma_{Max}$ (MPa)** | **$E_t$ (MPa)** | **$\varepsilon_b$ (%)** |
|---|---|---|---|
| Duraform / DTM Sinterstation 2500 **[27]** | 35 | 1100 | 17 |
| PA 2200 - EOS GmbH / EOSINT P395 **[33]** | 51 | 2171 | 16 |
| Duraform / 3D Systems **[11]** | 45 | 1720 | 10 |
| PA 2200 - EOS GmbH / DTM Sinterstation **[34]** | 51 | 1758 | 21 |
| **HP's 3D High Reusability PA 12 / MJF (current study)** | 49 | 1246 | 16 |

## Conclusions

This study investigated the properties and mechanical performance of PA12 parts printed using a production scale, powder bed fusion process (HP Jet Fusion 3D 4200 printer). Printing times of approximately 7.5 hours were used to print a set of 108 parts, over a build volume of 380 x 254 x 350 mm.

Coupons were printed to evaluate the physical and chemical properties of the PA12 parts. Prior to evaluation, the coupons were glass-bead blasted in order to remove the loosely bound, un-fused, PA12 particles adherent to the coupon surface. The resultant finish was a rough, grainy morphology, with a minimum $R_a$ of 2.54 ± 0.42 µm and a maximum $R_a$ of 10.29 ± 2.81 µm. Using optical microscopy on cross sections of the coupons, a porosity of 3.2 ± 4.1 % was obtained. The printed PA12 polymer exhibited similar chemical and thermal properties to results reported for this polyamide in the literature.

Mechanical testing was carried out based on tensile (ISO 527-1:2012) and flexural (ISO 178:2010) test measurements. To investigate the isotropy of the parts, three build orientations were investigated. The PA12 parts exhibited isotropic behaviour in terms of tensile strength. Based on the examination of fractured samples after tensile testing, the failure mode observed was moderately ductile. The parts exhibited a minor increase in tensile strength in the Z orientation, in comparison the X orientation. The printed PA12 parts exhibited a maximum tensile strength ($\sigma_{Max}$), and tensile modulus ($E_t$) values of 49 and 1246 MPa respectively. In terms of flexural testing, the build orientations had a significant effect on the strength of the printed part. The Z orientation had a 40% increase in flexural strength, when compared to that of the X orientation. The maximum flexural strength ($\sigma_f$), observed was 70 MPa with a modulus ($E_t$) of 1687 MPa.

While a direct correlation cannot be obtained with other PBF processing techniques for PA12, it was concluded from a literature review that mechanical properties of the printed parts are within the range of those reported for other production scale printing processes. The homogeneity of the printed parts as well as the processing speed indicates that the MJF™ process has enormous potential to facilitate the wider adoption of 3D printing in a production environment.

## Acknowledgements:

The authors would like to acknowledge the following: Henkel Ireland for supplying the printed parts, the support of the SFI funded MaREI Centre (12/RC/2302) and the I-Form Advanced Manufacturing Research Centre (16/RC/3872). The IR spectral acquisition was supported by the European Commission under the 7th Framework Programme (Grant agreement no:335508).

## References


1. Berman, B., *3-D printing: The new industrial revolution.* Business Horizons, 2012. **55**(2): p. 155-162.
2. Wendel, B., et al., *Additive Processing of Polymers.* Macromolecular Materials and Engineering, 2008. **293**(10): p. 799-809.
3. Standards, N., *Additive manufacturing - General principles -Terminology (ISO/ASTM 52900:2015)*, in *I.S. EN ISO/ASTM 52900:2017*. 2017.
4. Quinlan, H.E., et al., *Industrial and Consumer Uses of Additive Manufacturing: A Discussion of Capabilities, Trajectories, and Challenges.* Journal of Industrial Ecology, 2017. **21**(S1): p. S15-S20.
5. Hague *, R., S. Mansour, and N. Saleh, *Material and design considerations for rapid manufacturing.* International Journal of Production Research, 2004. **42**(22): p. 4691-4708.
6. Q. Sun, G.M.R., C.T. Bellehumeur and P. Gu, *Effect of processing conditions on the bonding quality of FDM polymer filaments.* Rapid Prototyping Journal, 2008. **14**(2): p. 72 - 80.
7. Hewlett-Packard. *HP MJF Website*. [cited 2017 8/12/17]; © Copyright 2017 HP Development Company, L.P.
8. Benedict. *3D printer and 3D printing news - www.3ders.org*. [cited 2016 05/01/18]; BMW to use new HP Jet Fusion 3D printer for serial part production & personal customization.
9. Zhu, W., et al., *A novel method based on selective laser sintering for preparing high-performance carbon fibres/polyamide12/epoxy ternary composites.* Sci Rep, 2016. **6**: p. 33780.
10. Vasquez, G.M., et al., *A targeted material selection process for polymers in laser sintering.* Additive Manufacturing, 2014. **1-4**: p. 127-138.
11. Salazar, A., et al., *Monotonic loading and fatigue response of a bio-based polyamide PA11 and a petrol-based polyamide PA12 manufactured by selective laser sintering.* European Polymer Journal, 2014. **59**: p. 36-45.
12. Hon, K.K.B. and T.J. Gill, *Selective Laser Sintering of SiC/Polyamide Composites.* CIRP Annals, 2003. **52**(1): p. 173-176.
13. Chung, H. and S. Das, *Processing and properties of glass bead particulate-filled functionally graded Nylon-11 composites produced by selective laser sintering.* Materials Science and Engineering: A, 2006. **437**(2): p. 226-234.
14. Goodridge, R.D., et al., *Processing of a Polyamide-12/carbon nanofibre composite by laser sintering.* Polymer Testing, 2011. **30**(1): p. 94-100.
15. Mazzoli, A., G. Moriconi, and M.G. Pauri, *Characterization of an aluminum-filled polyamide powder for applications in selective laser sintering.* Materials & Design, 2007. **28**(3): p. 993-1000.
16. Van Hooreweder, B., et al., *Microstructural characterization of SLS-PA12 specimens under dynamic tension/compression excitation.* Polymer Testing, 2010. **29**(3): p. 319-326.
17. Ellis, A., C.J. Noble, and N. Hopkinson, *High Speed Sintering: Assessing the influence of print density on microstructure and mechanical properties of nylon parts.* Additive Manufacturing, 2014. **1-4**: p. 48-51.
18. Griessbach, S., R. Lach, and W. Grellmann, *Structure–property correlations of laser sintered nylon 12 for dynamic dye testing of plastic parts.* Polymer Testing, 2010. **29**(8): p. 1026-1030.
19. Drummer, D., D. Rietzel, and F. Kühnlein, *Development of a characterization approach for the sintering behavior of new thermoplastics for selective laser sintering.* Physics Procedia, 2010. **5**: p. 533-542.
20. Kabalnov, A.S., J.T. WRIGHT, and V. Kasperchik, *Three-dimensional (3d) printing*. 2016, Google Patents.
21. D. K. Owens, R.C.W., *Estimation of the Surface Free Energy of Polymers.* Journal of Applied Polymer Science, 1969. **13**(8): p. 1741 - 1747.
22. Standards, N., *Plastics - Determination of tensile properties - Part 1: General principles (ISO 527-1:2012).*
23. Standards, N., *Plastics - Determination of flexural properties (ISO 178:2010).*

24. Wypych, G., *Handbook of Polymers.* ChemTec Publishing, 2012(PA-12 polyamide-12): p. 239 - 243.
25. Van Hooreweder, B. and J.-P. Kruth, *High cycle fatigue properties of selective laser sintered parts in polyamide 12.* CIRP Annals, 2014. **63**(1): p. 241-244.
26. Rhee, S. and J.L. White, *Crystal structure and morphology of biaxially oriented polyamide 12 films.* Journal of Polymer Science Part B: Polymer Physics, 2002. **40**(12): p. 1189-1200.
27. Caulfield, B., P.E. McHugh, and S. Lohfeld, *Dependence of mechanical properties of polyamide components on build parameters in the SLS process.* Journal of Materials Processing Technology, 2007. **182**(1-3): p. 477-488.
28. Salmoria, G.V., et al., *Mechanical properties of PA6/PA12 blend specimens prepared by selective laser sintering.* Polymer Testing, 2012. **31**(3): p. 411-416.
29. Starr, T.L., T.J. Gornet, and J.S. Usher, *The effect of process conditions on mechanical properties of laser-sintered nylon.* Rapid Prototyping Journal, 2011. **17**(6): p. 418-423.
30. Dizon, J.R.C., et al., *Mechanical characterization of 3D-printed polymers.* Additive Manufacturing, 2018. **20**: p. 44-67.
31. Goodridge, R.D., C.J. Tuck, and R.J.M. Hague, *Laser sintering of polyamides and other polymers.* Progress in Materials Science, 2012. **57**(2): p. 229-267.
32. Zarringhalam, H., C. Majewski, and N. Hopkinson, *Degree of particle melt in Nylon-12 selective laser-sintered parts.* Rapid Prototyping Journal, 2009. **15**(2): p. 126-132.
33. crHofland, E.C., I. Baran, and D.A. Wismeijer, *Correlation of Process Parameters with Mechanical Properties of Laser Sintered PA12 Parts.* Advances in Materials Science and Engineering, 2017. **2017**: p. 1-11.
34. Wegner, A. and G. Witt, *Correlation of Process Parameters and Part Properties in Laser Sintering using Response Surface Modeling.* Physics Procedia, 2012. **39**: p. 480-490.